Characterisation of Graphite Nanoplatelets (GNP) prepared at Scale by High-Pressure Homogenisation

Valentina Guerra[1], Chaoying Wan[1], Volkan Degirmenci[2], Jeremy Sloan[3], Dimitris Presvytis[4], Michael Watson[4], Tony McNally[1]*

[1]*International Institute for Nanocomposite Manufacturing (IINM), WMG,* [2]*School of Engineering and,* [3]*Department of Physics, University of Warwick, CV4 7AL, UK*

[4]*Thomas Swan & Co. Ltd, Consett, County Durham, DH87ND, UK*

*Corresponding author. Tel: +442476573256, E-mail: t.mcnally@warwick.ac.uk (Tony McNally)

Abstract

Graphite nanoplatelets (GNP) were prepared by a high-pressure homogenisation process (HPHP) via exfoliation of bulk graphite, yielding GNP in the form of square shaped platelets with lateral dimensions on the micrometre (μm) scale and thicknesses on the nanometre (nm) scale (<200nm). The platelets have a polycrystalline structure with d_{002}=0.335 nm and L_{002}=2nm, with a low crystalline defect concentration confirmed by weak D and D́ bands in the Raman spectra. The shift in the G band from 1587 cm^{-1} (graphene) to 1580 cm^{-1} (GNP) and the asymmetric Ǵ band combined with a decrease in $I_{Ǵ}/I_G$ from 0.45 for the bulk graphite to 0.40 for the GNP confirmed a partially exfoliated structure. X-Ray photoelectron spectroscopy (XPS) confirmed the presence of impurities on the GNP surface due to the surfactant used during the exfoliation process. Contact angle measurements (67° ±2° (0s), 64°±2° (10s)) suggested the surface of the GNP was hydrophilic. The as produced GNP is a macro-porous material with sheet-like particles having non-uniform shape and size and a BET surface area of *ca* 94 m^2/g. The GNP is thermally stable under oxidative conditions up to 430°C. The HPHP process is readily scalable and provides a cost effective route for the production of GNP.

Keywords: graphite nanoplatelets; high-pressure homogenisation process; exfoliation; characterisation, large scale

View Article Online
DOI: 10.1039/C9TC01361J

1. Introduction

Graphene is a two-dimensional (2D) layered material having a honeycomb like structure of sp^2-hybridized carbon atoms arranged in regular hexagons. The π-conjugation confers extraordinary mechanical, electrical and thermal properties, which continues to drive increasing and intense research interest in both academia and industry [1]. Graphene can be wrapped to create 0D fullerenes, rolled into 1D nanotubes or stacked to form a few layer structure (2-5 layers), a multilayer structure (5-10 layers), nanoplatelets (GNP, thickness less than 100nm) up to 3D structures (graphite), where the interlayer bonding is mainly due to Van der Waals interactions with a bond energy of 0.35 eV[2].

From composites with polymer matrices, to transistors, electrochemical systems, strain sensors, electronics, super-capacitors, hydrogen storage and solar cells, graphene and graphenic materials may find application in a vast number of industrial sectors [1, 3-10]. Since it continues to be difficult to obtain a perfect single layer graphene on an industrial scale, there is also a focus on GNP structures, which display many similar properties to graphene mono/multilayers [11]. To date, different procedures have been adopted to prepare GNPs, such as mechanical exfoliation, chemical vapour deposition (CVD), liquid phase exfoliation, electrochemical exfoliation, chemical reduction of graphene oxide (GO) and thermal exfoliation of acid-intercalated graphite [12-24]. However, all have limitations with regard manufacture at scale.

In this paper, we report for the first time, the properties of GNP prepared at scale (many tens of Kgs) by a high pressure homogenisation process (HPHP) with particular focus on surface and morphology characterization, determination of crystalline structure and thermal stability.

2. Experimental

2.1. GNP preparation via high pressure homogenisation

GNPs were prepared by Thomas Swan Ltd using a proprietary process, high-pressure homogenisation (HPHP), which is readily scalable, of bulk graphite. In this process, a solid suspension of bulk graphite in the particle size range 1μm to 1000μm is pumped at a pressure of > 1MPa and conveyed and directed via conduit towards an impact head having a surface

View Article Online
DOI: 10.1039/C9TC01361J

either off-set or directly perpendicular to the fluid flow direction. The conduit and impact head are arranged so that there is an annular gap of between 1μm and 500μm resulting in the fluid being temporarily constrained before exiting this area. The HPHP has significant advantages over all other exfoliation methodologies, most significantly, at scale. Indeed, delamination of graphite and a range of 2D nanomaterials has been achieved at pressures less than those used in micro-fluidisers, minimising heat build-up during processing. For the HPHP, production efficiency has been shown to be inversely proportional to temperature. The procedure is described in detail in [25].

2.2. GNP characterization

The characterization of the as produced GNPs was performed using a combination of techniques. Scanning Electron Microscopy (SEM), Transmission Electron Microscopy (TEM), X-Ray Diffraction (XRD) and Raman spectroscopy were chosen to study the morphology and the crystalline structure of GNP. X-ray Photoelectron Spectroscopy (XPS), sessile testing and nitrogen physio-sorption measurements were performed to investigate the surface properties of the GNP. Thermo-gravimetric analysis (TGA) was used to assess the oxidative thermal stability of the GNP, critical if such GNPs are to melt blended with polymers to form composite materials.

A Zeiss Sigma field emission instrument, fitted with a Gemini column, was used for the SEM imaging. The experiments were set with the InLens detector, a working distance of 3.2 mm and an acceleration voltage of 5 kV. A carbon adhesive tape was attached on the SEM stub before placing the samples, which were sputter coated (10nm) to minimize the charging on the surface of the sample. For that purpose, a Pd/Pt metal target (Cressington 108 auto) provided with a thickness controller was used.

TEM images were obtained using a FEI Talos F200X microscope allowed the TEM imaging. GNP were sonicated for 5 mins in chloroform before placing a few drops of the prepared dispersion on a Lacey carbon coated 200 mesh copper grid (Agar scientific). The grid was left at room temperature (RT) to completely dry.

A PANalytical Empyrean X-ray diffractometer (Wide-angle X-ray diffraction (WAXD)), was used to analyse the crystalline structure of the GNP. The instrument was

equipped with a Co ($K_{\alpha 1}$ (λ) = 1.789 Å) source, a PIXcel^{3D} detector, a tube voltage of 45 kV and current of 40 amps. The tests were set in reflectance mode with a stage of 1 rps speed. The sample in powder form was inserted in a coated Ni steel holder with a few mm thickness and 27mm diameter. The powder was pressed to a smooth and regular surface.

Raman measurements were carried out with a Renishaw inVia^{TM} Reflex confocal Raman microscope (Gonzo) (532 nm solid-state laser and x5, x20, x50 objectives). The instrument was fitted with a Renishaw CCD detector (Visible – NIR) and a 10 mW laser, which was spot focused on the sample with an exposure time of 2 mins and 5 collections.

A Kratos Axis Ultra delay-line-detector XPS instrument was used to characterize the surface of GNP. The instrument was equipped with a magnetic immersion lens and charge neutralisation system with spherical mirror and concentric hemispherical analysers. The survey spectra was collected using the Al K_{α} monochromatic ray (1.487 keV; emission=10 mA), with hybrid lens (aperture: slot), in the range of 0-1200 B.E. (steps of 1eV), 100ms dwell and 2 sweeps. The core spectra were collected using the Al K_{α} monochromatic ray (1.487 keV; emission=10 mA), with hybrid lens, in the range of 280-300 B.E for C1s and 526-550 B.E. for O1s (steps of 0.05eV), 400ms dwell and 50 sweeps. The sample orientation with respect to the detector was 90° whereas the nominal analysis area was 300µm x 700µm. The data collected were analysed using CasaXPS analysis software.

A Dyne Testing-ThetaLite instrument, fitted with a camera and a light source for optical measurements, was used to perform sessile tests on GNP. The pellet of GNP was positioned on the stage before placing a drop of distilled water (6 µL) onto the sample, using a manual dispenser. The measurements were carried out in five different points of the pellet and images recorded at RT over a time range of 10 s and

at 10% FPS. The software method set for the contact angle elaboration was based on Young-Laplace.

A Micromeritics ASAP2020 system was used to acquire nitrogen adsorption/desorption isotherms at -196°C on. GNP which was outgassed at 300°C for 4 h prior to the sorption measurements. The specific surface area was estimated by mean of Brunauer-Emmett-Teller (BET) equation in the range of relative pressure between 0.05 and 0.25.

The thermal stability of the GNP under oxidative conditions was studied in a Mettler Toledo TGA1-STARe system. The sample was placed in to 70 µL alumina pans and heated from RT to 800 °C at a constant heating rate of 10 K/ min. The resulting TGA and DTGA curves were plot in an x-y graph, where the y axis was normalized to unitary system in order to set a compatible scale for both TGA and DTGA values.

Electrical measurements were carried out using a 4-point probe conductivity meter (RM3000) with JANDEL cylindrical 4-point probe head to measure the sheet resistance of the GNP. The tests were performed on a water dispersion of GNP obtained from the HPHP. A convenient amount of the dispersion was diluted in deionised water (DI) and placed onto a Nylon membrane (diameter: 3.70 cm, thickness: 0.124mm). The membrane was washed with further DI before exsiccation in the oven at 50-60°C for 2h, to obtain a thin film of powder. The membrane was then weighed to calculate the amount of solid GNP before testing.

3. Results and discussion

Figure 1 (a-d) shows representative SEM images of the as produced GNPs.

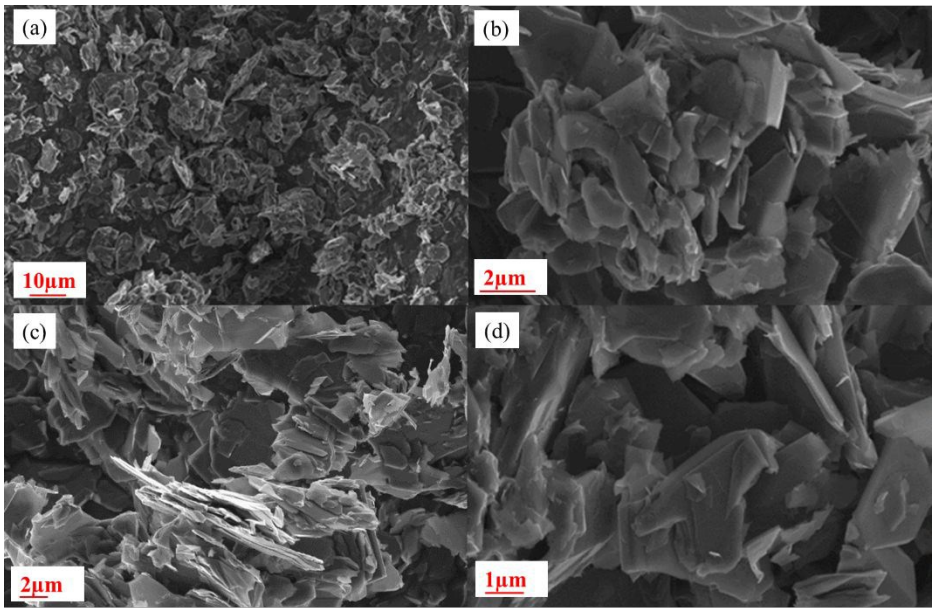

Figure 1. Scanning Electron Microsacopy (SEM) images of GNP at different magnifications.

GNPs present a multi-layered structure with irregular square-shape platelets agglomerating in clusters on the micrometre scale. The irregular flake-like structure of the GNP produced did not allow for a precise estimation of the dimensions of a single sheet, whose geometrical characteristics strongly depend on the type of fragmentation occurring during the HPHP process. [26]. We believe that bulk fragmentation is predominant during the exfoliation of graphite [26] and this is determined by the carbon-carbon bond energy. Indeed, graphite does not easily break along the carbon-carbon bond because of its partial double bond nature due to conjugation (C-C 348 kJ/mol, C=C 607 kJ/mol, in the gaseous phase at 298K) [27]. Therefore, a high number of large sheets exfoliate during HPP, which are realistically prone to break down further (bulk fragmentation) as they collide with each other rather than erode (edge fragmentation).

Figure 2 (a-e) shows the TEM images of GNP.

View Article Online
DOI: 10.1039/C9TC01361J

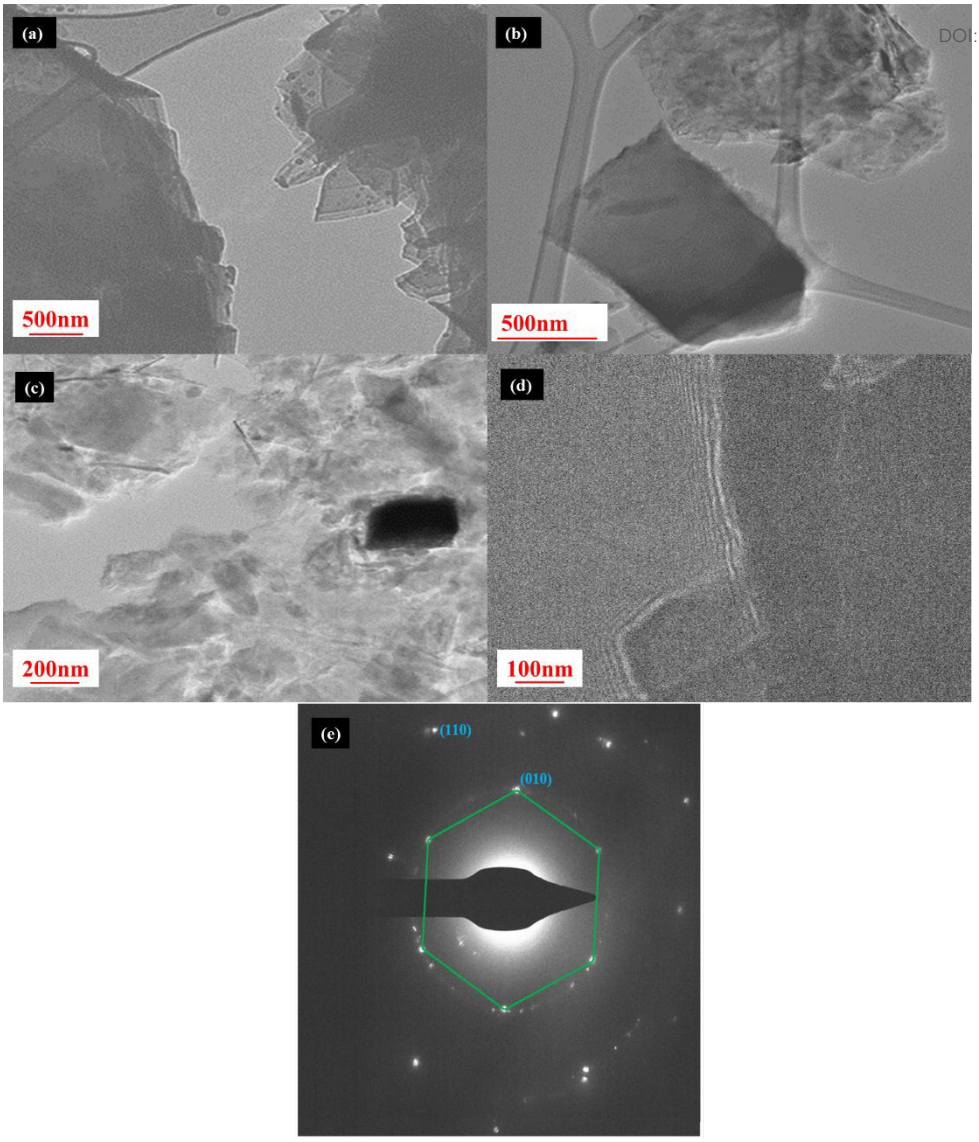

Figure 2. Transmission Electron Microscopy (TEM) images (a-d) at different magnifications. Selected Area Electron Diffraction (SAED) pattern (e) of the GNP. The hexagonal structure of GNP is evident from the drawn hexagon (green path) on the SAED image, which identifies the most intense flake (SAED taken from the image (d)).

A distribution of flake sizes with different transversal dimensions (thickness) were produced during HPHP as evident from the coexistence of few layer agglomerates (semi-transparent region) and thick clusters (dark regions) Figure 2(a-c). Some GNP sheets present curled edges (d) with a thickness of around 50 nm. The presence of square flakes, observed in the TEM images might be further confirmation that bulk fragmentation is the predominant step during the exfoliation process. The Selected Area Electron Diffraction (SAED) pattern in

Figure 2 (e) shows the most intense diffraction planes, (010) and (110). The presence of light halos suggests a polycrystalline structure with flakes differently oriented from each other [28].

The crystalline structure of GNP and the starting graphite was also studied by X-Ray diffraction (XRD), and the results are shown in Figure 3.

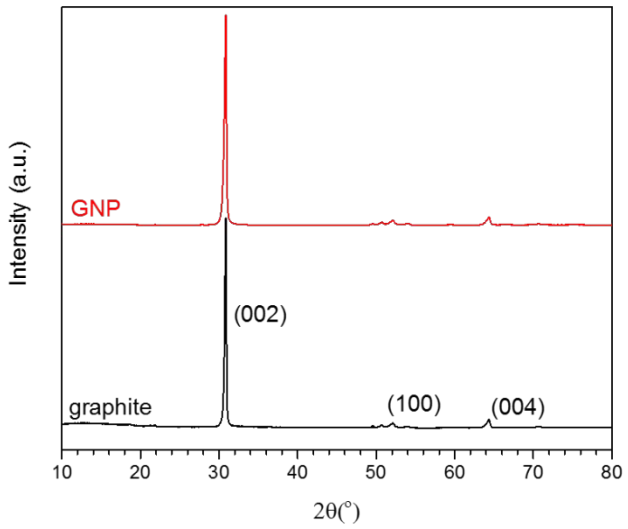

Crystalline planes/2θ	(002)/ 31°
	(100)/48.5°
	(004)/65°
$d_{(002)}$	0.335 nm
$L_{(002)}$	2 nm
N° crystalline planes (002)	6

Figure 3. X-Ray Diffraction (XRD) results of bulk graphite and GNPs. The interlayer distance along the crystalline plane (002) ($d_{(002)}$) was calculated from Bragg's law, whereas the thickness along the same plane ($L_{(002)}$) was estimated using Scherrer's equation. Further details about the XRD data elaboration procedure are reported in our previous work [29].

The XRD patterns reveal a highly crystalline material. The most intense and sharp peak observed at 2θ=31° is due to the crystallographic plane (002) of the graphitic structure. The crystallographic planes (100) and (004) generated the weaker peaks at 2θ= 53° and 65°, respectively. It should be noted that the different X-ray source used in this work (Cobalt, $\lambda_{CoK\alpha1}$= 1.789 Å) might lead to a slight shift of the peaks detected compared to the ones reported by other authors who typically use a Cu target [30]. No shift of the main crystallographic plane (002) is detected passing from the bulk graphite to the exfoliated material, that is, the ideal hexagonal unit cell is retained in the final product. Critically, the HPHP exfoliated graphite without damaging the crystalline structure. . The interlayer distance $d_{(002)}$ and the thickness $L_{(002)}$ are 0.335 nm and 2 nm respectively, in good agreement with values reported previously [30, 31]. This means that the peak at 2θ=31° is due to the contribution from six crystalline equidistant parallel planes (002).

View Article Online
DOI: 10.1039/C9TC01361J

The diffracted crystal planes registered in XRD ((002), (100), (004)) are different from the ones identified in SAED ((010), (110)). The shorter electron wavelength in SAED (λ_{SAED}= 0.00251Å, $\lambda_{CoK\alpha1;XRD}$ = 1.789Å) causes diffraction at smaller angles than in XRD. In other words, the diffracted rays from crystalline planes at the smaller angles recorded in SAED might not be recorded in XRD. Moreover, the multiple scattering in SAED, due to the stronger interactions of the matter with electrons than with X-rays, causes reflections is SAED, which are not registered in XRD.

Figure 4 shows the Raman spectra for bulk graphite and the GNPs.

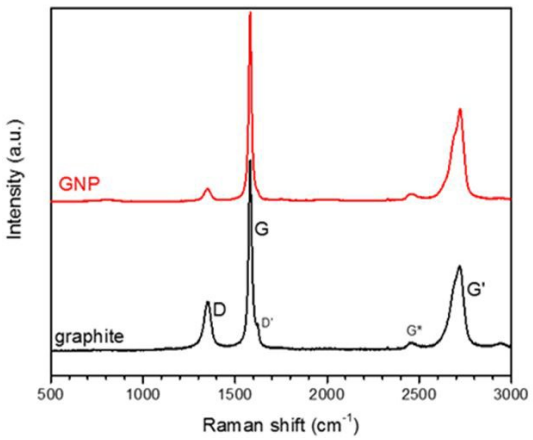

Material	Raman band	Raman shift (cm^{-1})
GNP	D	1350
	G (E_{2g})	1580
	D'	1650
	G*	2450
	G' (2D)	2700

Figure 4. Raman data for graphite and the as produced GNP.

Six peaks were identified in the Raman spectra at 1350 cm^{-1}, 1580 cm^{-1}, 1650 cm^{-1}, 2450 cm^{-1} and 2700 cm^{-1} due to D, G(E_{2g}), D́, G* and Ǵ(2D) bands, respectively [32]. Except for the G* band, the registered Raman bands in graphite and GNP are due to the scattering of optical phonons, which are in-phase (coherent) oscillations of atoms from their equilibrium position [33, 34]. The G band is the most intense due to elastic phonon scattering (first order Raman scattering), in particular, it refers to the doubly degenerate in-plane/out-of-plane vibrational modes of sp^2 hybridized carbon orbitals. The position and intensity of the G band yields information with regard the number of layers of the GNPs. Usually, the intensity increases linearly with the increasing number of layers and the peak shifts from 1587 cm^{-1} (monolayer) to 1580 cm^{-1} (multilayer structure) [11, 32]. In this case, the shift of the G band in the GNP spectrum is to 1580 cm^{-1} suggesting an exfoliated flake structure, confirming the formation of GNP and in agreement with accepted nomenclature for 2D carbon materials [35-38]. Furthermore, the ratio $I_{Ǵ}/I_G$ decreases from 0.45 for the bulk graphite to 0.40 for the GNP, confirming that the exfoliation of the bulk material occurred during the HPHP [39].

The D and Ḍ bands are associated with elastic and inelastic phonon scattering near a crystal defect (second order Raman scattering). In this case, these bands are quite weak suggesting that a low concentration of GNP defects in the crystal lattice was produced during the exfoliation process. The Ǵ band is due to phonon-phonon inelastic scattering (second order Raman scattering), and its symmetry gives information about the number of layers. A single layer produces a symmetric peak and the symmetry decreases with increasing number of layers [32]. For the GNP analysed in this work, the Ǵ band is slightly decentred suggesting an exfoliated flake structure. This result is in agreement with the conclusions made with regard the G band and our observations from SEM and TEM imaging.

The origin of the G* band in GNPs is still under investigation. Previous studies ascribed G* to a double resonance phenomenon, in particular, to a combination of both optical and acoustic phonon modes, where the latter is defined as out-of-phase (incoherent) oscillations of atoms from their equilibrium positions [33, 34].

X-Ray Photoelectron Spectroscopy (XPS) was used to study the chemical composition of the GNP surface. Figure 5 shows the representative peaks for GNP, whereas in Table 1 lists the main features identified from the analysis of the carbon (C1s) spectra.

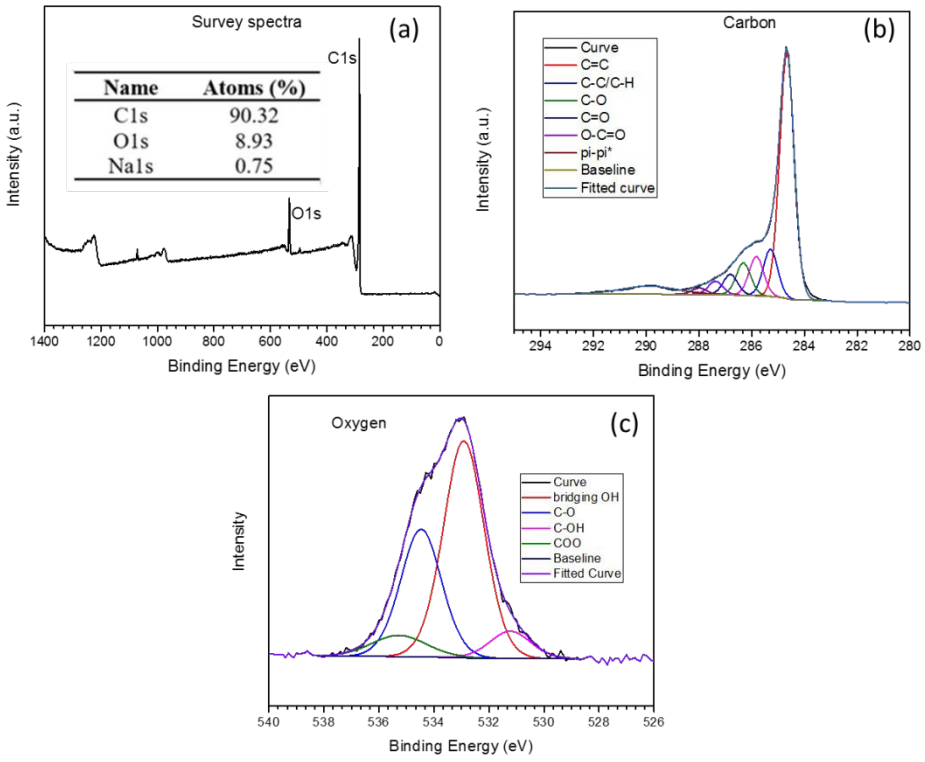

Figure 5. X-Ray Photoelectron Spectroscopy (XPS) results of GNP. Survey spectra (a), higher resolution core-level photoemission spectra of carbon (C1s) (b), and oxygen (c).

View Article Online
DOI: 10.1039/C9TC01361J

Table 1. Summary and assignment of XPS peaks identified for C1s in GNP.

Material	Detected atoms	Main Peaks	Lorentzian/Gaussian components
GNP	C1s	284 eV	C=C (284.6 eV) C-C/C-H (285 eV) C*-O (285.8 eV) C*=O (286.3 eV) O-C*=O (286.8) π-π* (290 eV)
	O1s	532.5 eV	NA
	Na1s	1071 eV	NA

The XPS survey spectra of the GNP identifies (a) C1s, O1s and Na1s at 284eV, 532.5eV and 1071eV, respectively [30]. The impurities from both the atmosphere and the surfactant (sodium cholate) used during the exfoliation process introduced oxygen and sodium atoms to the GNP surface. The higher resolution core-level photoemission spectra of C1s (b) shows an asymmetric and broad peak for carbon, suggesting that it is involved in a very complex bonding scheme. Indeed, the C1s spectra was fitted with six curves, a combination of Lorentzian/Gaussian profiles (GL(30) line-shapes, FWHM=0.638 except for the sixth curve (π-π*) whose FWHM is 2.452). The main curve at 284.6 eV is due to C=C bonding, followed by C-C/C-H at 285eV, C-O at 285.8eV, C=O at 286.3eV, O-C=O at 286.8eV and π-π^* at 290eV [30]. The C-C/C-H, C-O, C=O, O-C=O bonds can be associated with the interaction between GNP and the surfactant and eventually by the surfactant still present in trace amounts. This is supported by the presence of sodium in the survey spectra, derived from sodium cholate. Furthermore, the complex de-convoluted scheme of the higher resolution core-level photoemission O1s spectra supports the hypothesis of the surface impurities due to the presence of sodium cholate [40].

The surface of GNP was also analysed by performing sessile tests with distilled water as reference liquid. The results, registered over a time span of 10 s, showed a change of the contact angle from 67°±2 °at 0 s to 64°±2° at 10 s, revealing a hydrophilic surface for the GNP, as expected from the presence of carboxyl and hydroxides groups (see XPS). Figure 6 shows the contact angle images taken at 0 s and 10 s for GNP.

View Article Online
DOI: 10.1039/C9TC01361J

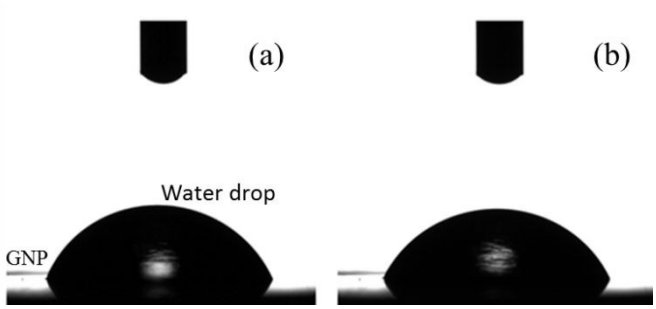

Figure 6. Contact angle images of GNP with water as the reference liquid taken at 0 s (a) and 10 s (b).

Further surface characterization of GNP was carried out by the nitrogen physio-sorption at -196°C. The adsorption and desorption isotherms are shown in Figure 7.

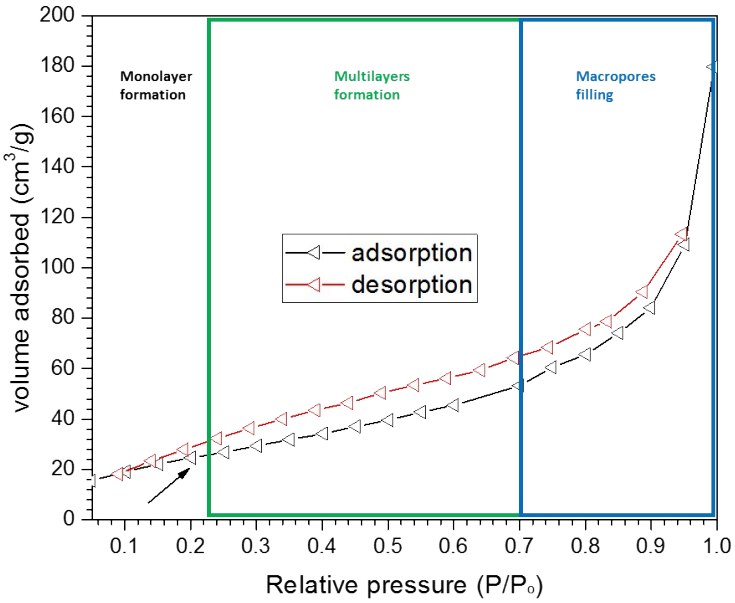

Figure 7. Nitrogen adsorption (black curve) and desorption (red curve) isotherms of GNP. The graph shows the regions were a monolayer of adsorbate is formed (black arrow), as well as the formation of multilayers (green zone) and the macro-pore filling region (blue zone).

The N_2 adsorption/desorption isotherms of the GNP obtained from the HPHP are typical of macroporous materials [41] (Type II, IUPAC classification). At a relative pressure of *ca* 0.25 a complete nitrogen monolayer is formed on the GNP surface, whereas at a relative pressure of *ca* 0.25-0.7 (quasi-linear region) the formation of nitrogen multilayers occurs. The filling of macro-pores ultimately caused the rapid increase of the isotherm at relative pressures above 0.7 and no condensation occurs.

The specific surface area of the GNP is *ca* 94 m^2/g, calculated using the Brunauer-Emmet-Teller (BET) equation in the range of relative pressure 0.05-0.25. The reported

desorption curve shows hysteresis [41](Type H3, IUPAC classification) and it is due to slit-like pores formed by the aggregation of sheet-like particles having non-uniform shape and/or size, in agreement with our observations from SEM and TEM images. The irregular geometry of the pores, the change of pore volume, the swelling of non-rigid pores, the irreversible uptake of nitrogen in the pores and the chemisorption caused the low-pressure hysteresis. For such reasons, the isothermal adsorption/desorption technique cannot be used to accurately study the pore size distribution of this GNP [41, 42]. Further details about the theoretical principles of physio-sorption applied to Type II materials are reported in our previous work [29].

The thermal stability of GNP under oxidative conditions was evaluated by Thermo-Gravimetric Analysis (TGA), see Figure 8.

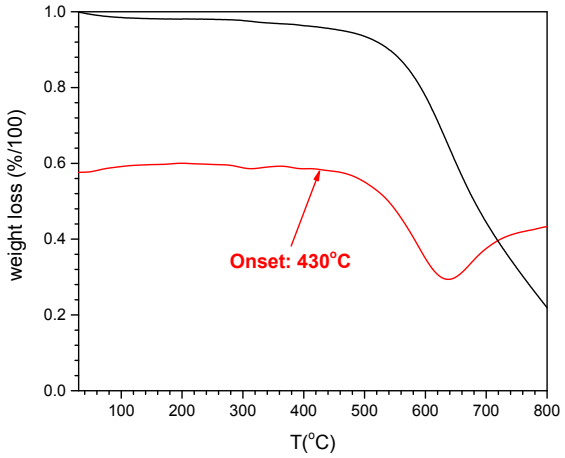

Figure 8. Thermo-Gravimetric Analysis (TGA) of GNP under oxidative conditions from 25°C to 700°C at 10 K/min. Weight loss (%/100) (black) and the first derivative (DTGA) (red) as a function of temperature T(°C).

The onset of the inflection point in the TGA weight loss curve (black), which corresponds to the onset decrease of the main peak in the DTGA curve, was used to identify the onset of degradation. The GNPs were relatively thermally stable under oxidative conditions and did not start to degrade until *ca.* 430°C. The weight loss registered below the degradation point (*ca.* 2 wt%) is due to residual water remaining after the exfoliation process. It is not possible to identify an end degradation (plateau) in the temperature range explored suggesting the GNP continued degrading above 800°C. At that temperature, the residue recorded was around 22wt%.

Sheet electrical resistance measurements were conducted on the dispersion of GNP out of the homogeniser, before drying, see Table 2.

View Article Online
DOI: 10.1039/C9TC01361J

Table 2. Electrical resistance of GNP from HPHP.

Material	Thickness (mm)	Sheet resistance (Ω/square)	Normalized sheet resistance to 25µm (Ω/square)
GNP (before drying)	0.040	23±2	37±3

The relative high sheet electrical resistance of the GNP is derived from the presence of the surfactant, agglomeration and voids formed upon deposition of the dispersion on the Nylon membrane.

4. Conclusions

The high-pressure homogenisation process (HPHP) was very effective at exfoliating bulk graphite to obtain graphite nanoplatelets (GNP). Table 3 summarises the properties of the GNP produced using this approach.

View Article Online
DOI: 10.1039/C9TC01361J

Table 3. Summary of the properties of GNP.

Technique	Results
SEM	nm thick flakes µm length sheets
TEM	Thin and thick flakes coexistence
SAED	Polycrystalline structure
XRD	$2\theta=31^{o}$ → (002) d_{002} = 0.335 nm L_{002} = 2 nm
Raman	1580 cm^{-1} → G -exfoliated flake structure D and D' band weak→low defects concentration G' (2D) slightly decentred → exfoliated flake structure
XPS	Carboxyl and hydroxides groups formation onto GNP surface; presence of surfactant residue
Sessile test	Contact angle: 67°±2°(0 s) 64°±2°(10 s)
N_2 ads./des. Isotherms **BET**	Macroporous material; slit-like pores Surface area: 94 m^2/g
TGA	Degradation onset (under oxidative conditions): 430°C
Sheet electrical resistance	37 □/m^2 (normalized at 25µm)

View Article Online
DOI: 10.1039/C9TC01361J

SEM imaging of GNP revealed a flake-like structure with square-shape sheets on the micrometre length scale, whereas from TEM imaging both few layered flakes and thicker aggregates were observed. SAED showed the typical hexagonal structures of GNP with polycrystalline flakes. The most intense and sharp peak at $2\theta=31^{\circ}$ (crystallographic plane=(002)) in the XRD pattern revealed a highly crystalline structure. This peak is associated with an interlayer distance of 0.335nm (Bragg's law) and dimension L_{002} (thickness of *ca* 2 nm (Scherrer equation) and it is due to six crystalline equidistant parallel planes (002). Raman spectra revealed an exfoliated flake structure (G band shift to 1583 cm^{-1}, G' band slightly asymmetric) having a low concentration of crystalline defects (weak D and D' bands). XPS analysis proved the presence of impurities on the GNP surface mainly due to sodium cholate, a surfactant utilised during the exfoliation process. This results in a slight functionalization of the GNP surface, as evident from the presence in XPS carbon spectra of carboxyl and hydroxide functional groups, which results in a hydrophilic GNP surface. This observation was confirmed from the sessile tests results of the GNP surface which revealed a contact angle of 67°±2° (0 s) and 64°±2° (10 s). The produced GNP is a macroporous material as confirmed by the nitrogen adsorption/desorption isotherms, where slit-like pores are formed by the aggregation of sheet-like particles having non-uniform shape and/or size. The BET the surface area of the GNP was calculated to be *ca* 94 m^2/g. The TGA of GNP showed high resistance to thermal degradation under oxidative conditions (T_{onset}=430°C). The sheet electrical resistance of the GNP (37 Ω/m^2) has a contribution from both residual surfactant and GNP flake agglomeration.

Acknowledgments

VG thanks the EPSRC (Grant No. EP/L016389/1) and Thomas Swan & Co Ltd for funding an EngD studentship. The authors thank Dr Jaipal Gupta, Dr Marc Walker, Dr Samuel Marks, Miss Syeda S. Abbas and Mr Martin Worrall for technical assistance. J. S. is indebted for support to the EPSRC from Grant No. EP/R019428/1.

References

[1] Potts JR, Dreyer DR, Bielawski CW, Ruoff RS. Graphene-based polymer nanocomposites. Polymer. **2011**,52:5-25.

[2] Papageorgiou DG, Kinloch IA, Young RJ. Graphene/elastomer nanocomposites. Carbon. **2015**,95:460-84.

[3] Schwierz F. Graphene and beyond: Two-dimensional materials for transistor applications. In: George T, Dutta AK, Islam MS, editors. Micro- and Nanotechnology Sensors, Systems, and Applications Vii2015.

[4] Bunch JS, van der Zande AM, Verbridge SS, Frank IW, Tanenbaum DM, Parpia JM, et al. Electromechanical resonators from graphene sheets. Science. **2007**,315:490-3.

[5] Raju APA, Lewis A, Derby B, Young RJ, Kinloch IA, Zan R, et al. Wide-Area Strain Sensors based upon Graphene-Polymer Composite Coatings Probed by Raman Spectroscopy. Adv Funct Mater. **2014**,24:2865-74.

[6] Eda G, Chhowalla M. Chemically Derived Graphene Oxide: Towards Large-Area Thin-Film Electronics and Optoelectronics. Adv Mater. **2010**,22:2392-415.

[7] Yoo JJ, Balakrishnan K, Huang JS, Meunier V, Sumpter BG, Srivastava A, et al. Ultrathin Planar Graphene Supercapacitors. Nano Lett. **2011**,11:1423-7.

[8] Patchkovskii S, Tse JS, Yurchenko SN, Zhechkov L, Heine T, Seifert G. Graphene nanostructures as tunable storage media for molecular hydrogen. Proceedings of the National Academy of Sciences of the United States of America. **2005**,102:10439-44.

[9] Wang X, Zhi LJ, Mullen K. Transparent, conductive graphene electrodes for dye-sensitized solar cells. Nano Lett. **2008**,8:323-7.

[10] Miao XC, Tongay S, Petterson MK, Berke K, Rinzler AG, Appleton BR, et al. High Efficiency Graphene Solar Cells by Chemical Doping. Nano Lett. **2012**,12:2745-50.

[11] Allen MJ, Tung VC, Kaner RB. Honeycomb Carbon: A Review of Graphene. Chem Rev. **2010**,110:132-45.

[12] Papageorgiou DG, Kinloch IA, Young RJ. Mechanical properties of graphene and graphene-based nanocomposites. Prog Mater Sci. **2017**,90:75-127.

[13] Novoselov KS, Geim AK, Morozov SV, Jiang D, Zhang Y, Dubonos SV, et al. Electric field effect in atomically thin carbon films. Science. **2004**,306:666-9.

[14] Yu QK, Lian J, Siriponglert S, Li H, Chen YP, Pei SS. Graphene segregated on Ni surfaces and transferred to insulators. Appl Phys Lett. **2008**,93:113103/1-3.

[15] Zhang Y, Zhang LY, Zhou CW. Review of Chemical Vapor Deposition of Graphene and Related Applications. Acc Chem Res. **2013**,46:2329-39.

[16] Suk JW, Kitt A, Magnuson CW, Hao YF, Ahmed S, An JH, et al. Transfer of CVD-Grown Monolayer Graphene onto Arbitrary Substrates. ACS Nano. **2011**,5:6916-24.

[17] Li XS, Magnuson CW, Venugopal A, Tromp RM, Hannon JB, Vogel EM, et al. Large-Area Graphene Single Crystals Grown by Low-Pressure Chemical Vapor Deposition of Methane on Copper. J Am Chem Soc. **2011**,133:2816-9.

[18] Hernandez Y, Nicolosi V, Lotya M, Blighe FM, Sun ZY, De S, et al. High-yield production of graphene by liquid-phase exfoliation of graphite. Nat Nanotechnol. **2008**,3:563-8.

[19] Blake P, Brimicombe PD, Nair RR, Booth TJ, Jiang D, Schedin F, et al. Graphene-based liquid crystal device. Nano Lett. **2008**,8:1704-8.

[20] Park S, An JH, Jung IW, Piner RD, An SJ, Li XS, et al. Colloidal Suspensions of Highly Reduced Graphene Oxide in a Wide Variety of Organic Solvents. Nano Lett. **2009**,9:1593-7.

[21] Paredes JI, Villar-Rodil S, Martinez-Alonso A, Tascon JMD. Graphene oxide dispersions in organic solvents. Langmuir. **2008**,24:10560-4.

[22] Abdelkader AM, Cooper AJ, Dryfe RAW, Kinloch IA. How to get between the sheets: a review of recent works on the electrochemical exfoliation of graphene materials from bulk graphite. Nanoscale. **2015**,7:6944-56.

[23] Low CTJ, Walsh FC, Chakrabarti MH, Hashim MA, Hussain MA. Electrochemical approaches to the production of graphene flakes and their potential applications. Carbon. **2013**,54:1-21.

[24] Wang GX, Yang J, Park J, Gou XL, Wang B, Liu H, et al. Facile synthesis and characterization of graphene nanosheets. J Phys Chem C. **2008**,112:8192-5.

[25] Ladislaus Paul GL, McHale Ronan. C01B 31/04 (2006.01) ed2017. p. 1-11.

[26] Liscio A, Kouroupis-Agalou K, Betriu XD, Kovtun A, Treossi E, Pugno NM, et al. Evolution of the size and shape of 2D nanosheets during ultrasonic fragmentation. 2d Materials. **2017**,4.

[27] Dean JA. *Lange's Handbook of Chemistry*. fourteeth ed. New York: McGraw-Hill, Inc.; 1999.

[28] Liu JB, Li PJ, Chen YF, Wang ZG, Qi F, He JR, et al. Observation of tunable electrical bandgap in large-area twisted bilayer graphene synthesized by chemical vapor deposition. Scientific Reports. **2015**,5.

[29] Guerra V CW, Sloan J, Degirmenci V, Presvytis D, McNally T. 2D Boron Nitride Nanosheets (BNNS) Prepared by High-Pressure-Homogenisation: Structure and Morphology. Nanoscale. **2018**,10:19469-77.

[30] Stobinski L, Lesiak B, Malolepszy A, Mazurkiewicz M, Mierzwa B, Zemek J, et al. Graphene oxide and reduced graphene oxide studied by the XRD, TEM and electron spectroscopy methods. J Electron Spectrosc Relat Phenom. **2014**,195:145-54.

[31] Li YM, Tang LH, Li JH. Preparation and electrochemical performance for methanol oxidation of pt/graphene nanocomposites. Electrochem Commun. **2009**,11:846-9.

[32] Malard LM, Pimenta MA, Dresselhaus G, Dresselhaus MS. Raman spectroscopy in graphene. Physics Reports-Review Section of Physics Letters. **2009**,473:51-87.

[33] Shimada T, Sugai T, Fantini C, Souza M, Cancado LG, Jorio A, et al. Origin of the 2450 cm(-1) Raman bands in HOPG, single-wall and double-wall carbon nanotubes. Carbon. **2005**,43:1049-54.

[34] Mafra DL, Samsonidze G, Malard LM, Elias DC, Brant JC, Plentz F, et al. Determination of LA and TO phonon dispersion relations of graphene near the Dirac point by double resonance Raman scattering. Phys Rev. **2007**,76:233407/1-4.

[35] Shao YY, Zhang S, Wang CM, Nie ZM, Liu J, Wang Y, et al. Highly durable graphene nanoplatelets supported Pt nanocatalysts for oxygen reduction. J Power Sources. **2010**,195:4600-5.

[36] Yadhukulakrishnan GB, Karumuri S, Rahman A, Singh RP, Kalkan AK, Harimkar SP. Spark plasma sintering of graphene reinforced zirconium diboride ultra-high temperature ceramic composites. Ceram Int. **2013**,39:6637-46.

[37] Monti M, Rallini M, Puglia D, Peponi L, Torre L, Kenny JM. Morphology and electrical properties of graphene-epoxy nanocomposites obtained by different solvent assisted processing methods. Compos Part A Appl Sci Manuf. **2013**,46:166-72.

[38] Xiang JL, Drzal LT. Templated growth of polyaniline on exfoliated graphene nanoplatelets (GNP) and its thermoelectric properties. Polymer. **2012**,53:4202-10.

[39] Ramirez C, Osendi MI. Characterization of graphene nanoplatelets-Si3N4 composites by Raman spectroscopy. J Eur Ceram Soc. **2013**,33:471-7.

[40] Liu P, Wang J, Qi W, Li Z, Bi JJ, Wu WS. Adsorption of Eu(III) on oMWCNTs: Effects of pH, Ionic Strength, Solid-Liquid Ratio and Water-Soluble Fullerene. Journal of Nanomaterials. **2013**.

[41] Leofanti G, Padovan M, Tozzola G, Venturelli B. Surface area and pore texture of catalysts. Catal Today. **1998**,41:207-19.

[42] Sing KSW, Everett DH, Haul RAW, Moscou L, Pierotti RA, Rouquerol J, et al. Reporting Physisorption Data For Gas Solid Systems With Special Reference To The Determination Of Surface-Area And Porosity (Recommendations 1984). Pure Appl Chem. **1985**,57:603-19.

View Article Online
DOI: 10.1039/C9TC01361J

View Article Online
DOI: 10.1039/C9TC01361J

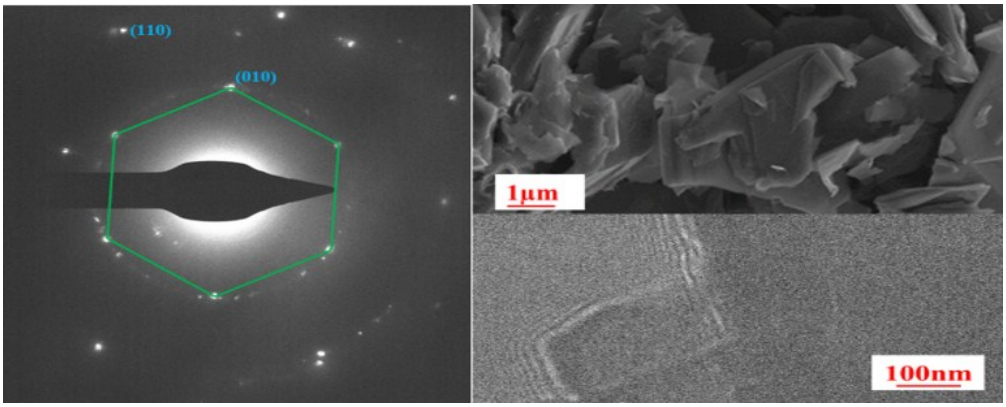

130x51mm (150 x 150 DPI)